Ocean Engineering 247 (2022) 110678

Contents lists available at ScienceDirect

Ocean Engineering

journal homepage: www.elsevier.com/locate/oceaneng

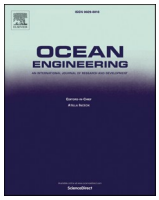

Integrated approach to assess resonance between basin eigenmodes and moored ship motions with wavelet transform analysis and proposal of operational thresholds

Raquel Costas [a,*], Andrés Figuero [a], Enrique Peña [a], José Sande [a], Paulo Rosa-Santos [b]

[a] Water and Environmental Engineering Group (GEAMA), University of A Coruña, Campus Elviña s/n, 15071, A Coruña, Spain
[b] Department of Civil Engineering, Faculty of Engineering, University of Porto, Rua Dr. Roberto Frias s/n, 4200-465, Porto, Portugal

ARTICLE INFO

Keywords:
Infragravity waves
Moored vessel motions
Wavelet transform analysis
Vessel resonance
Operational threshold

ABSTRACT

Waves with periods between 25 s and some minutes can amplify the motions of moored ships, which may result in terminal downtimes and compromise safety. The purpose of this work is twofold: (i) studying infragravity waves and their influence on moored ship motions, including the definition of operational thresholds and (ii) developing a novel and integrated approach to identify and assess resonance situations using wavelet transform analysis. The resonant modes of the harbor basin were identified using a numerical model validated with full-scale data. The motions of five similar LPG vessels moored at two adjacent jetties were analyzed, both in the frequency and frequency–time domains. It was concluded that surge is the most important motion at the berth that has greater operational problems. Moreover, the infragravity motion periods vary with the mooring line pretension and are proportional to the ratio *of water depth* to *vessel draft*. Three episodes of mooring line breaking were attributed to large infragravity surge oscillations. In addition, operational thresholds for basin-vessel resonance situations were defined based on the port tide gauge data. A significant wave height of 0.075 and 0.010 m for the 30–65 s period band was established for LPGs and oil tankers, respectively.

1. Introduction

The growth in international maritime trade in recent decades is undeniable, estimated at 4 billion and 11.08 billion tons in 1990 and 2019, respectively, despite the contraction of global merchandise trade in the latter owing to the slowdown in the world economy (UNCTAD, 2020). Accordingly, ports compete to offer more efficient and safer services (Molavi et al., 2019). In general, the conditions for ports' (un) loading operations depend fundamentally on the behavior of the moored vessel. Large amplitude motions of moored ships reduce operational efficiency and security, interrupt cargo handling, and induce the breaking of mooring lines, among others (Tharanga, 2014; van Dongeren et al., 2016). Horizontal motions are often responsible for operational problems. Their natural period is usually in the infragravity band (25 s–150 s), and hence, are driven by infragravity waves.

Physical modeling is widely applied to the analysis of moored ship behavior under short waves (Rosa-Santos et al., 2014; Santos et al., 2019). The effects of long waves are more limited (Yoneyama et al., 2004; Shi et al., 2014), and have been addressed using numerical models with different approaches. Gap resonance and harmonics between two identical fixed rectangular boxes have been studied in Zhao et al. (2017) and Wang et al. (2019). Resonance and infragravity oscillations in moored vessel motions have been studied in Pohang Harbor, South Korea (Kwak and Pyun, 2013; Kumar et al., 2016) and in Geraldton Harbor, Australia (Gourlay, 2019). In terms of operational efficiency, numerical simulations were also conducted in the work of González-Marco et al. (2008). Minimizing long-wave amplification in new port designs or the application of dynamic mooring systems is a potential solution to prevent this problem (van Deyzen et al., 2015). However, implementing them in built harbors is not always possible. Other developments focus on identifying the safest mooring locations under resonant conditions based on amplification factors (Kumar and Gulshan, 2018; Gao et al., 2020) and providing recommendations on mooring configurations (Troch et al. (2020), for example, in Cape Town, South Africa.

Traditionally, in both numerical models and field studies, analyses have been performed in the frequency domain with a stationary and average approach by using fast Fourier transforms. Because long waves

* Corresponding author.
E-mail address: raquel.costas.gomez@udc.es (R. Costas).

https://doi.org/10.1016/j.oceaneng.2022.110678
Received 15 July 2021; Received in revised form 3 November 2021; Accepted 22 January 2022
Available online 3 February 2022

have non-stationary and non-periodic characteristics, Díaz-Hernández (2006) proposed wavelet transform analysis (WTA). This recommended method allows the study of records in the frequency–time domain. The use of WTA is especially suitable for the analysis of moored vessel dynamics, as most of the parameters that control the ship response vary with time, such as the tide level, vessel draft/loading, mooring configuration, and pretension. For instance, Gulshan et al. (2020) stated that increasing the ratio *of water depth* to *vessel draft* decreases the amplitude of the resonant peaks. Therefore, a specific study of moored vessel motions in the frequency–time domain allows identification of the amplification of the motions, the involved variables, and the potential consequent incidents.

Full-scale measurements of moored ship motion are limited in the literature and usually refer to one or a few ships. In some cases, data were used to compare or validate numerical models (Troch et al., 2020). In other cases, specific problems such as long waves (Hiraishi, 1997; Uzaki et al., 2010) were analyzed. In the case of the inner port of A Coruña, Spain, previous studies (Figuero et al., 2019) analyzed motion thresholds from the current literature and estimated the responses of the moored vessels based on measurements. López and Iglesias (2014) conducted an investigation at the outer Port of Ferrol, Spain, which emphasizes the need to establish a threshold for low-frequency wave energy, although this has not been accomplished yet. Existing thresholds are summarized in works such as PIANC (1995) and Spanish ROM 2.0–11 (Puertos del Estado, 2011). These are based on the allowed amplitudes of the vessel motions, which are usually unknown.

Despite the studies and implications of long-period motions, the identification and evaluation of basin-vessel resonance situations remain a challenge. In the interviews of port stakeholders conducted in Sasa et al. (2018), 65% of the responders experienced cargo handling or ship mooring problems owing to infragravity vessel motions. Moreover, 59% of them perceive that the current situation is not satisfactory enough to maintain safety at harbors. The low-frequency response of ships moored with an asymmetric mooring system could be induced by resonance between the surge motion and long-period waves or harbor oscillations (Sakakibara and Kubo, 2008). Resonance can be triggered throughout the loading process, and adding extra mooring lines may result in larger vessel motions (Bhautoo, 2017). Moreover, the proximity of the ship to a basin node is likely to result in larger amplitudes of motion (Troch et al., 2020). Problems strongly depend on the environmental conditions and characteristics of each port (such as bathymetry, geometry, berth location, weather conditions, and water level), as well as the loading condition, mooring pretension and configuration, and vessel typology. Furthermore, different ships have different allowable motions depending on the cargo handling equipment. This means many variables are involved, making it difficult to identify the cause of these problems. Consequently, the availability of real (full-scale) data is essential.

Based on the above observations, this work presents an integrated approach to assess the infragravity motions of moored vessels, enabling it to be applied at any port. This methodology was tested at the oil terminal of the inner port of A Coruña (Spain). Consequently, the hydrodynamics at the selected berths were analyzed based on sea-surface data measured at three different locations. In addition, the resonant modes of the basin were obtained by applying a numerical model. Based on the port operators' experience, one jetty is more prone to downtime problems than the other. The vessel motions were studied in the spatial–frequency domain by comparing the spectra of five measured motions of five analogous liquefied petroleum gas (LPG) vessels at two close locations. Consequently, the effects of different wave conditions and mooring configurations were investigated. Furthermore, to detect resonance phenomena, surge motion was analyzed in the time-frequency domain (WTA), along with the concomitant waves. Finally, time information was obtained for eight downtimes of vessels at four mooring locations. Wave heights in the different frequency bands of the sea states corresponding to these interruptions were analyzed. Consequently, operational thresholds for basin-vessel resonance situations were proposed for different types of berths.

The remainder of this paper is arranged as follows: Section 2 presents the material and methods used. Section 3 presents the results of the hydrodynamic analysis. Section 4 describes the vessel motion study in the spatial–frequency and temporal–frequency domains, along with the proposed operational thresholds for basin-vessel resonance. Finally, the conclusions are presented in Section 5.

2. Material and methods

2.1. Study area: San Diego oil terminal of the inner port of A Coruña (Spain)

The inner port of A Coruña is on the western side of the river mouth of A Coruña in northwest Spain (43°21′27.6″ "N; 8°23′13.7"″ W) (Fig. 1a). This location is exposed to one of the most adverse meteorological conditions in Europe because of the presence of low-pressure systems in the mid-Atlantic Ocean (Lorente et al., 2018). Puertos del Estado (Spanish National Port Authority) buoy (Fig. 1b) shows an annual average significant wave height, H_s, of 1.6 m, which corresponds to a non-exceedance probability of 0.5. Moreover, an annual average storm event is 6 m significant wave height, H_s, and a winter average storm event of 7 m, both corresponding to a no exceedance probability of 0.995. Additionally, the maximum tidal range is 4.50 m. As regards the wave directions, the major directions are NNW, NW, and WNW, where NW is the direction of the most extreme conditions. Consequently, the inner port was built inside the river mouth of A Coruña and was protected by a 1.330 m long breakwater.

The different docks inside the port are reserved for each sector of activity, including three marinas, a multi-purpose terminal, a cruise terminal, two fishing terminals, two general cargo terminals, and an oil terminal (San Diego); the latter is the subject of this study (see Fig. 1c). The analyzed basin occupies an estimated water surface area of 321.000 m^2, where the oil terminal has four jetties. Jetties 1 and 2 have an average depth of 12.5 m, where gas and chemical tankers dock. Jetties 3 and 4 have a deeper draft of 16 m and are used as oil tankers.

2.2. Field campaign

The field campaign entailed the simultaneous collection of moored ship motion data during cargo operations and sea-surface oscillations. In addition, the mooring line configuration, time sheets of each monitored vessel, one loading log, and one damage stability booklet were available. Information about the accurate time of the eight downtimes and the corresponding tide gauge records was also obtained. These correspond to different vessels berthed at the four jetties.

The measurements of the sea-surface elevation were made using two types of devices: one tide gauge and two pressure sensors. Fig. 1d shows the locations of the three gauges. The two pressure sensors were installed at each side of the oil terminal, and data were recorded at a frequency of 1 Hz. The tide gauge, (Miros radar), was installed at the center of the studied terminal with a record frequency of 2 Hz. Additionally, hourly data of wave parameters outside the port (Fig. 1c) were obtained from the propagation point CORUÑA (43° 24′ 48″ N 8° 23' 00" W) of the official Spanish wave propagation network. In the days of

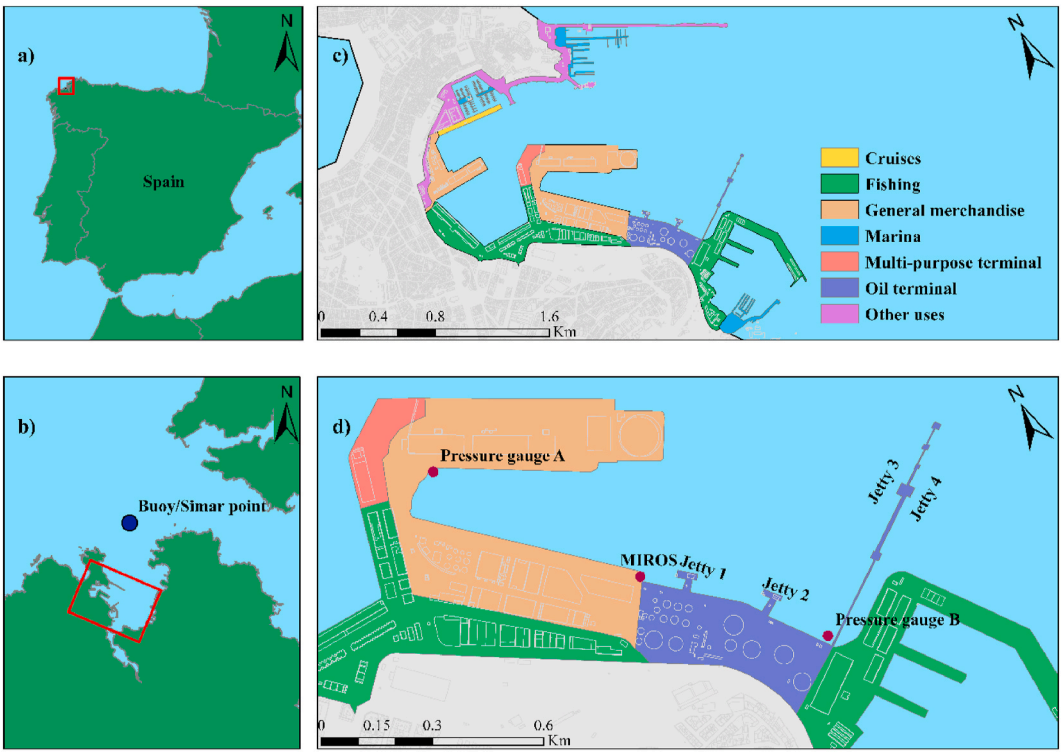

Fig. 1. (a) Iberian Peninsula showing A Coruña location, (b) river mouth of A Coruña and the port location, (c) Plan view of the Inner Port of A Coruña, and (d) location of the measuring equipment and jetties in the San Diego oil terminal of Port of A Coruña. Source of soil occupancy: SIOSE (Information System on Soil Occupancy in Spain) assigned by © National Geographic Institute–Government of Galicia.

Table 1
Vessels and details of the monitoring campaign. Mooring lines in the following order: Lines (fore-aft), spring lines (fore-aft), and breast. Vessel drafts in the following order: arrival-departure.

Vessels		Monitoring data			Vessel drafts	
ID	Name	Jetty	Total time	Mooring lines	Fore	Aft
ST_A	Scali del Teatro	1	14 h	3-3-3-3	3.40–5.80	4.90–6.00
SSL	Scali Sanlorenzo	2	6 h 40 min	3-3-3-3 + (1 fore - 2 aft)	3.55–5.55	5.20–5.75
ST_B	Scali del Teatro	1	18 h 20 min	3-3-3-3	3.85–5.00	4.70–5.60
ST_C	Scali del Teatro	2	19 h 20 min	3-3-2-2	3.10–4.90	4.60–5.60
SR	Scali Reali	2	11 h 40 min	3-3-3-3	3.90–4.90	4.90–5.80

unavailable data, numerical model data (Simar point 213099004) at the same location were used. Miros radar, CORUÑA, and Simar points belong to the Spanish National Ports Authority (Puertos del Estado, 2021).

Conversely, moored ship motions were recorded in jetties one and two, as shown in Fig. 1d, using two different devices: an inertial measurement unit and an optical motion tracking system. The mode of operation of both measuring systems is described in Figuero et al. (2018a), and their validation is presented in Figuero et al. (2018b). Here, five LPG vessels with the same dimensions 88 m × 15 m x 5 m (overall length, beam, and draft) under different maritime climates were selected. It should be noted that three of them are literally the same ship, and all of them were loaded during their stay at the port. The purpose was to eliminate the variability that would be introduced into the analysis by comparing different ships. A summary of the reference vessels and their operational characteristics are presented in Table 1. Furthermore, Table 2 shows the average maritime climate data, corresponding to short waves, inside and outside the port, and tidal range during the monitoring time of each ship.

Table 2
Average maritime climate data during vessel monitoring time. (*Average maritime climate from numerical model data (Simar point 213099004)).

Vessel ID	Propagation buoy			Miros radar	
	H_s (m)	T_p (s)	Dir (º)	H_s (m)	Tidal range (m)
ST_A	3.9	14.8	314	0.29	2.69
SSL	3.8*	14.1*	306*	0.21	2.44
ST_B	2.2*	11.5*	321*	0.14	2.01
ST_C	1.0*	12.1*	324*	0.05	1.51
SR	3.0	10.1	316	0.12	1.64

2.3. Data analysis

2.3.1. MSP numerical model

To determine the natural periods of oscillation and the corresponding resonance modes of the inner port of A Coruña a numerical model based on the elliptical formulation of the mild slope equations was applied. These models can solve long waves and propagation phenomena (refraction, diffraction, shoaling, partial reflection, and wave radiation to the outside of the port). This is done through an adaptive finite element method (FEM) mesh and two-dimensional pattern solving.

The numerical model employed in this study was (MSP-IHCantabria)-IHCantabria (Mild Slope Ports). This model allows the analysis of port resonance from complex bathymetry and real contours. The

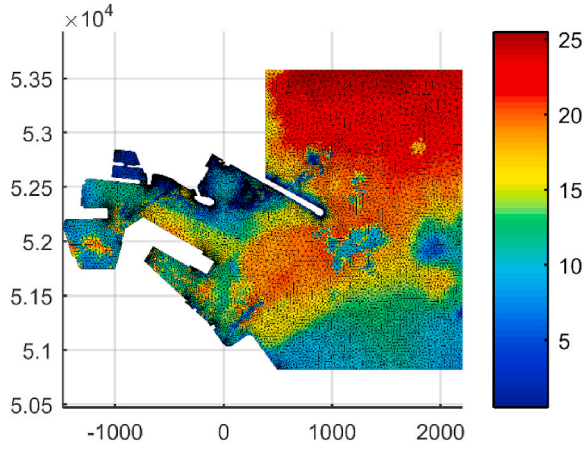

Fig. 2. Propagation FEM mesh generated with 30 s target period by MSP model in the Inner Port of A Coruña.

bathymetric data used were a combination of a bathymetric survey of the port and bathymetry of the river mouth. The first was provided by the Spanish National Ports Authority (Puertos del Estado, 2021) and the second was collected from the European Marine Observation and Data Network (EMODnet).

The boundaries were established through the coastline at sea level and the water contours to the wave generation zone, which was located at 0.5 wavelength from the first obstacle. As regards the major objective of this analysis (resonance study), the reflection coefficient used was 1, except for the water contours, which were assigned a value of 0. After characterizing the contour, the model generated a propagation mesh. It uses the FEM with growth as a function of bathymetry; therefore, more detail is obtained in the shallower areas (Fig. 2). Consequently, a design period of 30 s (the smallest of the propagated cases) was defined.

A total of 270 cases of regular waves were propagated on the mesh from the center point of the open contour. These were selected by performing a period sweep from 30 to 300 s, along with a wave height of 0.25 m. The direction was north, perpendicular to the generation contour. From the physical perspective, it should be noted that wave-breaking, white-capping, and nonlinear quadruplet wave-wave interactions were disabled.

The output was not only the wave height maps that locate the nodes and antinodes but also the resonant periods and the amplification factor at the selected locations. Here, it was obtained at the locations of the pressure sensors and the (Miros radar). For normalization of the results, they were multiplied by four because the input of wave height was 0.25 m. To evaluate the influence of tides, the model was run three times by changing the boundary shape for different water levels: mean higher high water (MHHW), mean lower low water (MLLW), and mean sea level (MSL).

Hence, when the MSP model was used and the port bathymetry and geometry considered, it was possible to estimate the natural periods of oscillation and amplification factors in the inner port. Specifically, low-frequency oscillations occurred in the vicinity of the oil terminal. These results were validated with the two wave gauges of the outermost zone of the basin (Fig. 1d), the gauges next to the studied jetties. Accordingly, the maps that show the location of the nodes and antinodes can be used to analyze the influence of basin resonance on vessel motion at each jetty.

2.3.2. Fast Fourier transform (FFT)

FFT was applied to the time series to identify the energy peaks and the corresponding periods. This technique is widely used in different engineering fields, including this field of study. For instance, FFT was used in numerical, experimental, and measured surface signals (Leys et al., 2018) and moored vessel motions (Uzaki et al., 2010; Rosa-Santos et al., 2014).

In this study, FFT was used for the time series of wave gauges to validate the peak periods at each position obtained by the MSP. Furthermore, it was applied in a time series of ship motions to compare each motion between them and with waves. Therefore, the influence of wave energy and other variables on vessel motion could be studied. Finally, wave heights associated with different frequencies were obtained for the sea states that generated the recorded downtimes. Consequently, the wave heights were computed as $H_{m0} = 4\sqrt{m_0}$, where m_0 is the zero-order moment of the spectrum obtained by this method. It was calculated using the integral of the FFT results in the target frequency bands.

2.3.3. Wavelet transform analysis

The wavelet power spectrum is the transformation of a signal into an energy spectrum, such as the FFT. However, this method is advantageous in that, different period power packages are identified in time. Torrence and Compo (1998) developed a practical guide to its application, and Liu et al. (2007) made an improvement since it became the method energy and physically consistent, allowing a comparison of the spectral peaks across scales. This improved wavelet was applied because it enables the simultaneous identification of energy packages in terms of time and frequency through colors.

Spectrograms are a similar transform tool based on the short-time Fourier transform, and some authors, such as López et al. (2012) and García-Valdecasas et al. (2021) used it in wave climate analysis. However, the spectrogram used a fixed window length. Thus, WTA improves the high-frequency resolution (Loughlin and Cohen, 2010), which makes it a suitable transform to be applied to non-stationary signals. Consequently, the tool is increasingly used in many scientific fields such as medicine, finance, and engineering (Rhif et al., 2019). Massel (2001) and Huang (2004) applied it to wave climate analysis and Díaz-Hernández (2006) and Gao et al. (2020) employed it for numerical model gauge data. Yu et al. (2006) studied the modeled responses of the roll motion and its coupling with heave, where the feasibility of this tool is highlighted. It should be noted that other authors take advantage of this method for real-time roll motion prediction during navigation (Liu et al., 2020). More recently, Zhang et al. (2021) performed a forecast of the six degrees of freedom of a moored vessel by combining wavelet transform with a long short-term memory network. In prediction, it is applied to the decomposition of motions. Therefore, WTA is underutilized to study moored vessel motions and is unexplored in full-scale measurements.

The spectrum is generated through the convolution of the signal with a scaled and translated mother function. This means it adapts the window size to the frequency using longer windows for lower frequencies and shorter windows for higher frequencies. Different mother functions (wavelets) exist. In the case of sea oscillations and ship motions, the Morlet function was chosen because of its good performance demonstrated by its application to wave records (Massel, 2001; Huang, 2004). The wavelet transform was applied by adapting the procedure used by Liu et al. (2007). An initial scale of 4 s was established because shorter periods were not studied. The total number of scales specified was 111, ranging from 4 to 485 s. The values of the periods associated with each scale grew exponentially, such that for lower periods, the number of scales was greater.

The described tool was used to analyze the response of the concomitant (Miros radar) data and the motions of the selected ships. Therefore, a comparison of the period and energy variations with time was possible. Consequently, the influence of cargo, tide, and mooring line pretension was explored, as well as the basin-vessel resonance phenomenon.

3. Hydrodynamic results and discussion

To study the influence of waves on moored vessel motions, basin

hydrodynamics are analyzed in this section. The sea-surface oscillations were evaluated using the FFT to explore the frequency domain. Additionally, the inner port of A Coruña was modeled using MSP to determine the resonance periods in the studied locations and resonance maps. The obtained amplification factors were validated with measured data from the (Miros radar) and pressure gauge B owing to their proximity to the studied jetties.

To facilitate the analysis, the frequency band was divided into three parts, entailing three-period bands, as outlined below.

- Swell and wind waves (SW) with $f_- = 40$ mHz and $f_+ = 250$ mHz (4 s–25 s);
- Infragravity waves (IG) with $f_- = 6.6$ mHz and $f_+ = 40$ mHz (25 s–151 s);
- Far infragravity waves (FIG) with $f_- = 3$ mHz and $f_+ = 6.6$ mHz (151 s–333 s).

The FFT of the tide gauge (Miros radar,) records corresponding to the days of monitored vessels, for 24 h each, were compared (Fig. 3a). Same peak periods (45, 65, 90, and 260 s) were identified in low-frequency bands whereas short-wave peak periods range from 10.1 s to 14.8 s. In the absence of data outside the port, oscillations in the natural resonant periods of the basin are considered to be caused by the bound infragravity waves. These waves reaching the port may be in the entire spectrum without defined peaks, as in Thotagamuwage and Pattiaratchi (2014). They are associated with swell wave groups; therefore, the magnitude of long waves is affected by the short-wave intensity. The most energetic spectrum in the SW band remains at the other bands, and the fewest powerful record entails no peaks at higher frequencies. This latter corresponds to a 0.05 m of wave significant height, H_s, whereas, in the other days, H_s was at least 0.12 m (see Table 2). The wave direction might also be an influencing parameter; however, it is not possible to conclude as insufficient data were obtained. With more data points, mainly outside the port, a further study could be performed as in the work of Reniers et al. (2021).

Fig. 3b shows the FFT of the three available sensors from a 24 h record. They were located as shown in Fig. 1d: pressure gauge B was at the most external point of the basin, pressure gauge A at the most internal point, and (Miros radar) at an intermediate location. In the right band (SW), the more inner the location, the lower the energy of the waves, as expected. In the IG band, a 45 s period is noticeable at the (Miros radar), next to jetty 1. However, 65 s and 90 s appear from the three gauges, although at the intermediate, it is less energetic. The 150 s period became powerful in the outer gauge. Finally, in the peak period of 260 s (FIG), the inner pressure gauge showed the highest energy as opposed to the outer one, inversely to the SW band. This is because of the resonance modes, which will be analyzed in the resonance maps.

Hence, different periods and powers were identified at each location. In addition, the energy of the resonant frequency within the basin always exists under certain swell conditions. Here, it is verified that resonance peaks antinodes at the (Miros radar) occur when, at least, the short-wave significant wave height is equal to or greater than 0.12 m.

To study the resonant patterns that lead to moored vessel motions, the MSP outcomes were validated in the external points, (Miros radar), and pressure gauge B positions. These two devices were selected for being in the studied jetties. Fig. 4 describes the resonance periods and amplification factors obtained from the MSP model for the MSL condition. Furthermore, they were compared with the FFT of the measurement records for a period of 24 h. Whereas MSP results are plotted in terms of relative wave height, the records are plotted in terms of spectral density; thus, the comparison of the magnitude is only qualitative. However, the resonance period comparison was quantitative. The MSP results show that at more external pressure gauges, next to jetty 2, the spectral density peaks are highlighted at 65, 90, 150, and 260 s. In addition, at the (Miros radar) position, next to the jetty 1, 45, 90, and 260 s periods are noticed. Nonetheless, in the latter location, the numerical model results are not similar to the actual measurements in the IG frequency range. Two possible explanations exist for this finding. First, the bathymetry had a limitation; thus, the results could be improved by a larger detailed bathymetry covering the river mouth. Second, discrepancies could be at different levels. The results of the numerical model were exposed to the MSL, and the spectral density peaks were affected by the tide. The depth modifies the long-wave peak periods: higher tide levels lead to reduced resonant periods, and lower levels lead to an increase. For instance, the 45 s peak ranges from 40 s to 49 s, as shown in Fig. 5. The same applies to the 90 s peak range, which varies from 75 s to 95 s, in MHHW and MLLW, respectively.

A significant positive correlation exists between the resonant modes studied with the numerical model and the harmonic oscillations of the San Diego basin given by the theoretical formulations. The periods were obtained by:

$$T_n = \frac{2L}{n\sqrt{gH}} \text{ for a close basin} \tag{1a}$$

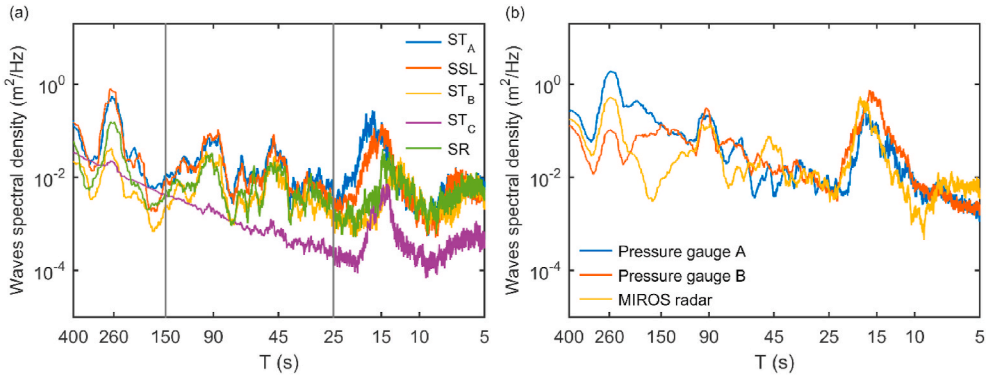

Fig. 3. (a) FFT of 24 h records of Miros radar for the days where the studied vessels were monitored (b) FFTs of concomitant 24 h record of Miros radar and pressure gauges.

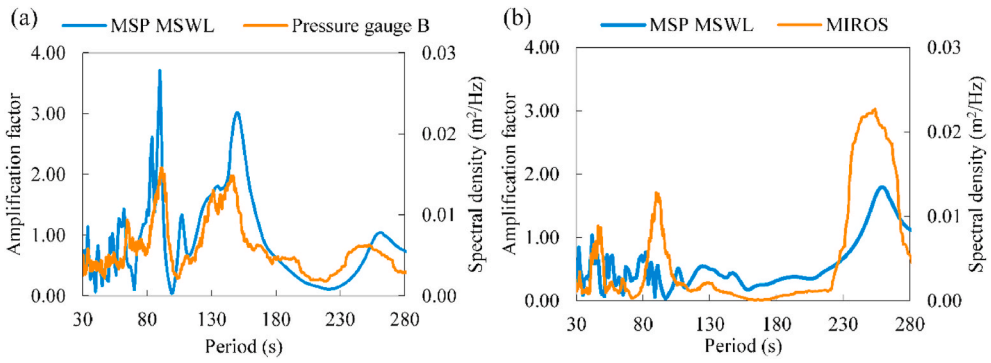

Fig. 4. Validation of the MSP model: (a) amplification factor from MSP and spectral density from pressure gauge B and (b) Miros radar.

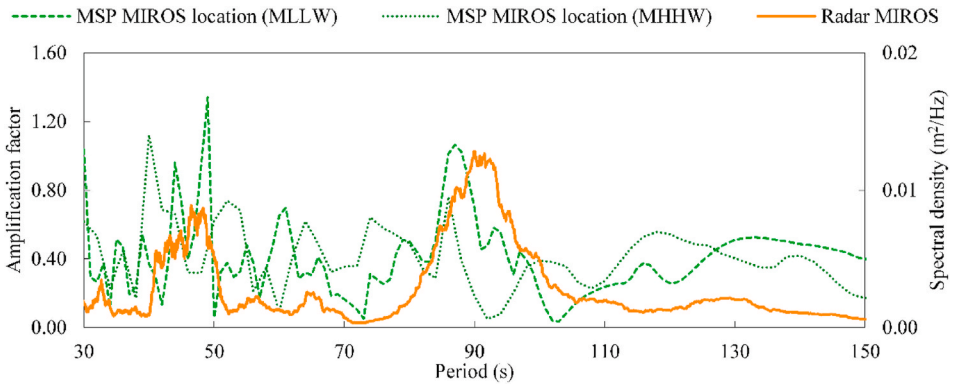

Fig. 5. Validation of the MSP model: amplification factor from MSP (MLLW and MHHW) and spectral density from Miros radar.

Table 3
Theoretical natural frequency modes for the open and closed basin, based on the length, width, and the distance between studied jetties and the main breakwater of the port (studied at two sea levels (MHHW- MLLW)).

Mode	Open basin			Closed basin		
	San Diego basin (width)	San Diego basin (length)	San Diego basin - main breakwater	San Diego Basin (width)	San Diego basin (length)	San Diego basin - main breakwater
1	28–25 s	120–136 s	141–159 s	37–42 s	181–203 s	181–203 s
2		72–81 s	85–95 s		90–102 s	90–102 s
3		52–58 s	60–68 s		60–68 s	60–68 s
4		40–45 s	47–53 s		45–51 s	45–51 s

$$T_n = \frac{4L}{(2n+1)\sqrt{gH}} \text{ for an open basin} \quad (2)$$

where the mode is defined by $n = 0, 1, 2, 3, \ldots$, L is the basin length or width, g is the acceleration owing to gravity, and H is the basin depth (Sorensen and Thompson, 2008). The San Diego basin width and length are calculated as the average, 240 m and 1.166 m, respectively; additionally, results were obtained for the distance between the main breakwater and the studied jetties (1.365 m); depth refers to the mean drafts at MHHW and MLLW. The results are summarized in Table 3.

The oscillation periods obtained for the east-west length of the oil terminal basin and the distance between the study berths and the main breakwater of the port (north-south) are similar, especially when using the closed basin formula. This occurs because both distances are similar. The 45 s resonant period matches the fourth mode, which is generated longitudinally, using the open-basin formulation. The 150, 90, and 65 s peak periods coincide with modes 1, 2, and 3, calculated with the length between the studied basin and the main breakwater when regarded as an open basin. The mode of 260 s was not obtained because it may be generated between the harbor and the east coast of the river mouth of A Coruña.

In conclusion of the validation results, the model reasonably predicts the frequency of the resonant modes; however, no conclusions can be drawn on the amplification factors. Thus, the model outcomes were considered appropriate for the resonance mode analysis, just as their influence on moored vessel motions.

The resonant mode maps (Fig. 6) show the amplification factor of the waves, identifying nodes (amplification factor near 0) and antinodes (maximum amplification factor), where the horizontal and vertical maximum velocity zones occur, respectively. The water motion in the

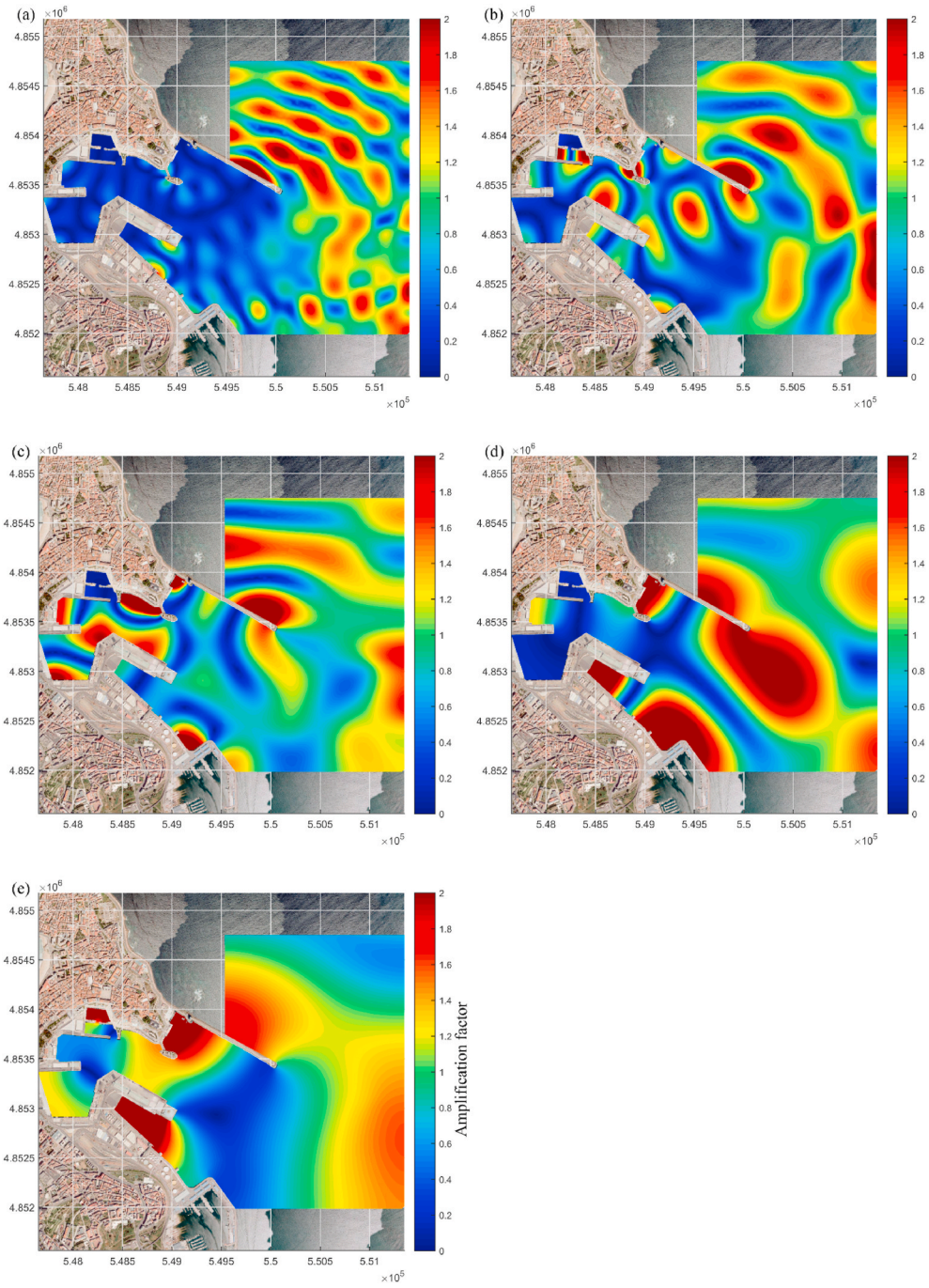

Fig. 6. Resonance modes corresponding to the wave periods of 45 s (a), 65 s (b), 90 s (c), 150 s (d), and 260 s (e), for the MSL.

basin can cause motion of the vessels; therefore, the corresponding maps with the peaks of maximum amplification in the vicinity of the moorings were analyzed. These peaks are the periods shown in Fig. 3b: 45, 65, 90, 150, and 260 s. As mentioned above, they are influenced by sea level; hence, Fig. 6 illustrates the corresponding maps for the MSL.

In the IG band, the 45 s eigenmode generates an antinode at the Miros radar location and another in the pressure gauge B position, which is less energetic. Therefore, the node is in the area of berths. Furthermore, the 65 s pattern presents the maximum amplification in the basin corners at the pressure gauge site. The last period in the IG frequency band is 90 s, the pattern of which is the vertical maximum speed at the location of pressure gauge B and the nearest jetty (jetty 2) with the same magnitude. However, it influences the other jetty and (Miros radar), although to a lesser extent, as shown in Fig. 3b.

The peak periods in the FIG frequency band were 150 s and 260 s, respectively. The 150 s mode has two antinodes, one at the external part

of the basin (pressure gauge B and jetty 2) and the other at the opposite position (pressure sensor A). This leads to the location of the node in the intermediate basin ((Miros radar) and jetty 1). Finally, the eigenmode corresponding to the 260 s peak shows an antinode in the innermost zone (pressure gauge A) and decreases toward the outermost zone (pressure gauge B). Consequently, the vertical amplification was greater in the inner dock.

Resonance modes in the vicinity of the berth lead to vessel motion. For this reason, determining nodes and antinodes allowed us to study the effect of infragravity hydrodynamics on ship motions, as presented next. In addition, the influence of the dock location was analyzed because the resonance patterns differ from jetty 1 to jetty 2, also identifying the basin-vessel resonance phenomenon at each berth.

4. Vessel results and discussion

In this section, the dynamic behavior of moored ships is analyzed and discussed based on hydrodynamic conditions. As discussed in Section 2.2, five LPGs with the same dimensions under different maritime climate conditions were studied. The natural surge periods were calculated for each ship and their motions were explored in the spatial–frequency domain (FFT). When the spectra obtained for the different vessels were compared, it was possible to identify the influence of the hydrodynamics (therefore berthing location) and mooring configuration on the moored ship response. Moreover, two of these five vessels, one for each jetty, were investigated in the temporal–frequency domain (WTA). Accordingly, in addition to the FFT analysis, the effect of parameters that vary over time, such as load condition, tide, and changes in mooring line pretension can be studied. Finally, operational thresholds for basin-vessel resonance based on available downtime and wave information were proposed.

4.1. Natural surge period

To verify the resonance between ships and the basin, the natural surge period of the analyzed vessels was estimated where the moored ship was considered as an ordinary mass-spring system, using the following formula:

$$T_n = 2\pi\sqrt{D_w/K} \tag{1b}$$

where D_w (t) is the displacement weight, and K (kN/m) represents the total spring constant of the mooring ropes. The first parameter (D_w) was estimated by interpolation using the information of drafts and displacements from the stability booklet of the Scali Sanlorenzo (SSL) and the real drafts of each vessel. To obtain the total spring constant (K), only the contribution of the moorings in the direction of the surge motion was considered. Natural periods were obtained for new and broken-in moorings. The results are summarized in Table 4.

The vessel with the least number of lines (ST_C) had longer periods in all combinations. Corresponding to new moorings, loaded vessels berthed at jetty 2 show longer maximum periods than vessels at jetty 1. Despite having the same mooring configuration, the lengths of the lines are greater in jetty 2 because of the bollard positions. It is worth mentioning that basin depth is not taken into account in this formula and has important implications, as shown by the wavelet transform.

4.2. Vessel motions: spatial–frequency analysis

In this section, the concomitant data of moored ship motions and wave records of the (Miros radar) are studied in the frequency domain through the FFT (Fig. 7). The short-wave band (SW band) directly affect the heave, roll, and pitch motions, which have natural periods of oscillation in the same frequency band, as proven by other authors such as López and Iglesias (2014). They also confirmed that surge, yaw, and sway motions present peak periods in the IG band. Thus, all motions of the referenced vessels were studied by comparing the wave energy and location. However, the impact of the mooring configuration was only analyzed for horizontal motions because they were the most directly affected.

For a better understanding, a comparison between the vessel behavior for similar wave conditions (*i.e.*, wave spectra) but berthed at different jetties, was performed. ST_A (jetty 1) and SSL (jetty 2) were monitored during the days with the most adverse maritime climate. SR (jetty 2) and ST_B (jetty 1) operated with intermediate wave conditions, and finally, ST_C was exposed to the lowest (see Table 2 and spectra in Fig. 7a).

First, the heave motion spectrum of all analyzed vessels is similar to the wave spectrum, mainly in the SW band, where peaks are the most powerful, as expected (Fig. 7a and b). In this band, vessels berthed at jetty 2 showed more heave spectral density, as they were more exposed (see Fig. 1d). As regards the IG band, when the two vessels docked during the most severe conditions are compared, energy is higher between 45 and 65 s. The wave spectrum presented two peaks (45 s and 65 s). This is achieved because of a greater variation in the motion period owing to the tidal range, which is greater in those days (Table 2).

In contrast, a 150 s peak is seen in the heave spectrum of the same vessels, displaying more energy than that berthed at jetty 2, where the antinode is located (Fig. 3b). Finally, the ship at the internal jetty presents a greater 260 s peak than the ship on account of the antinode at the basin innermost area, as the resonance mode is confirmed in Fig. 6e.

Analogously, the roll and pitch spectra in all periods remain proportional to the sea energy (Fig. 7c and d). In addition, the dominant peak is in the SW band, as observed in the heave motion, because these motions are governed by high-frequency waves. In the IG band, roll motion could be related to the heave because the shape of the spectrum is similar, particularly remarkable on vessels docked in days with the most adverse maritime climate. Therefore, heave can affect the roll in

Table 4
Natural surge periods of studied vessels depending on their displacement and cargo for new and broken-in moorings.

Vessel ID	Jetty	Average draft (m)		Estimated displacement weight (MT)		Natural surge periods (s)			
		Ballasted	Loaded	Ballasted	Loaded	Ballasted		Loaded	
						Broken-in	New	Broken-in	New
ST_A	1	4.15	5.90	3368	5539	16	35	20	44
SSL	2	4.35	5.65	3622	5066	16	39	19	46
ST_B	1	5.28	5.30	4639	4667	19	40	19	40
ST_C	2	3.85	5.25	3029	4610	19	40	24	48
SR	2	4.4	5.35	3650	4724	17	39	19	45

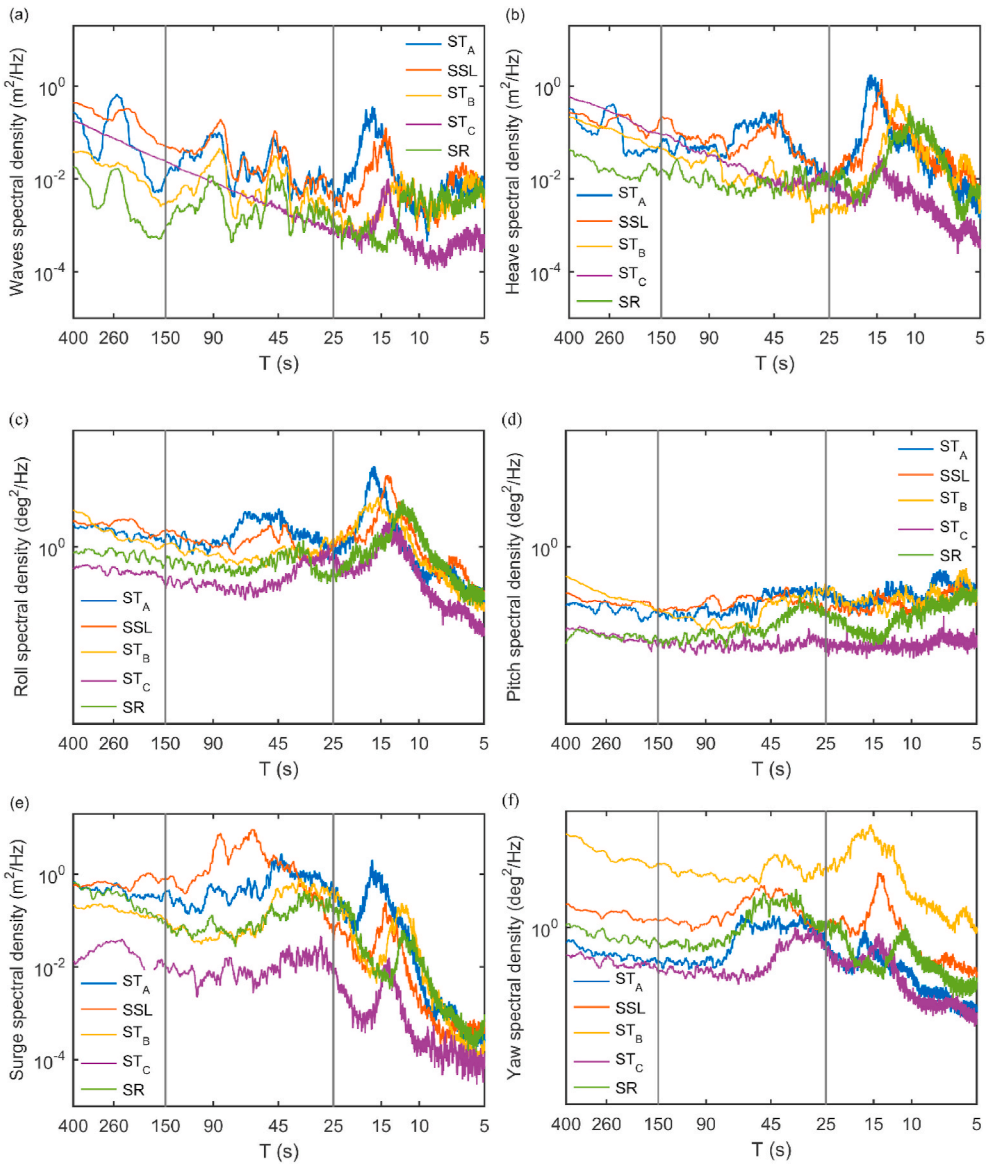

Fig. 7. FFT of the time series of (a) Miros radar waves, (b) heave, (c) roll, (d) pitch, (e) surge, and (f) yaw motions.

the IG band.

The natural periods of horizontal motions are in the IG band; therefore, infragravity waves can excite them. Moreover, they are highly conditioned by the mooring system; any modification of it will affect the oscillatory behavior. Thus, it was considered relevant in the surge and yaw analyses.

Focusing on the surge (Fig. 7e), the spectra of the vessels berthed at the inner jetty present more energy in the SW band. In addition, the peak periods are the same as those in the waves. In the IG band, the surge of all ships has the same spectrum shape, and the peak energy is between the natural surge period obtained (20–50 s). The exception is the SSL vessel (65–90 s peak), which has a more powerful spectrum than the other with the same sea energy. This vessel has a different mooring configuration, and pretension data are unavailable. Therefore, both could be responsible variables, since an asymmetry in the mooring system and line pretension affect the subharmonic motion considerably (Sakakibara and Kubo, 2008; van der Molen et al., 2006). In the last instance, the resonance between the basin and the moored ship could lead to this outcome. Hence, the surge motion of this ship was studied through a wavelet transform in the next section. When the pair of vessels with intermediate wave power and the same mooring configuration, 3-3-3-3 (see Table 1) was observed, the ship at the inner jetty suggests more energy at 45 s than the ship at the outer berth. These differences can be explained by the resonance patterns. The main antinode of 45 s was next to jetty 1 (Fig. 6a). Consequently, the influence was greater at the nearest berth.

In the FIG band, the surge of more exposed vessels increases their energy with respect to the others. This is connected to the resonance pattern because at nodes, horizontal motions are greater, and this jetty is closer to the 260 s node than the other, as shown in Fig. 6e.

As regards yaw, because this is a low-frequency oscillating motion, such as surge, its peak period is expected to be in the IG band, as three of the five vessels in Fig. 7f (45 s). However, the two ships present the peak period in the SW band, berthed at each jetty. These are the vessels with the highest energy along the entire spectrum, in contrast to the wave spectrum. In the case of the mooring configuration, one of these ships (SSL) is the only one with breast lines (see Table 1). Therefore, neither location, waves, nor moorings demonstrate an explanatory influence on the yaw amplitudes. The absence of mooring line pretension information is worth mentioning.

The port operators' experience indicates the inner jetty is more problematic for operability and safety than the outer jetty. In light of the preceding considerations, because vessels moored in the most protected location, jetty 1 presents higher surge energy in the SW and IG bands.

4.3. Vessel motions: temporal–frequency analysis

To study temporal variations in the frequency domain, WTA was applied. When the wavelet transform of waves and ship motions are compared, it is possible to analyze how variations in tide, loading condition, or moorings affect the behavior pattern of the ship at berth.

To study cargo variations, the loading process was analyzed. The loading log was available for the vessel Scali Reali (SR), which allowed us to check its linearity, as shown in Fig. 8. The calculation is based on the assumption that the vessel draft is only modified by loading and is not affected by the ballast, as no information is available to analyze its influence. Therefore, drafts of all ships were obtained during the loading process as a linear function of the total cargo quantity and time. It is assumed that this is valid for the referenced vessels because the loading method and supply were the same.

When the vessel draft and the basin depth are combined, the factor δ can be obtained as $\delta = water\ depth/vessel\ draft$. Therefore, the δ factor fits the tide curve with linear modifications owing to the cargo. Gulshan et al. (2020) demonstrated the importance of this factor on the resonant effects in a numerical model. They suggested that an increase in δ decreases the amplitude of the resonant peaks in Paradip Port, India, owing to the variation of added mass and damping with the under-keel clearance, which impacts the natural periods of the ship. The current study allows deeper analysis by considering the resonance behavior of the basin and the incoming low-frequency energy using measured data.

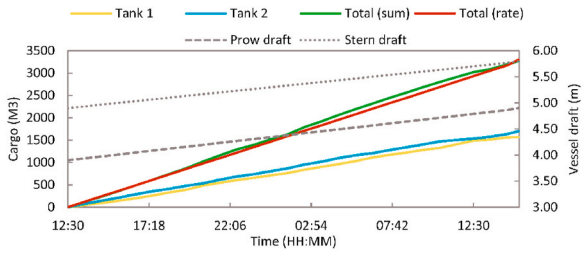

Fig. 8. Cargo and vessel draft evolution of SR on 11/06/2019 and 11/07/2019 at the outer jetty.

To examine these parameters and their influence on motion, two ships are studied in this section. The ST_B ship (jetty 1) checks the changes caused by the temporal evolution of variables such as the tide and the loading process, as it has the longest monitoring time. Second, the SSL (jetty 2), which suffered three mooring breaks and different behavior in the surge (see Fig. 7e).

To study the motions of the first vessel, ST_B waves from the Miros radar were analyzed. Fig. 9a shows the recordings corresponding to the SW, IG, and FIG bands obtained by applying a window filter between the frequencies of each band. The tide variation is represented in the secondary axis. The wavelet transform of the Miros radar record is shown in Fig. 9b. Finally, a comparison between the FFT and MSP results is plotted in Fig. 9c.

The perceived behavioral differences allow the division of Fig. 9 into three parts for a better understanding. These parts correspond to the first low tide, high tide, and second low tide. These divisions are highlighted by the black vertical lines.

The window filters of all frequency bands show a decrease in energy at the second low tide. This supports the hypothesis that IG and FIG oscillations are bound to infragravity waves associated with swell wave groups (in the absence of data outside the port). In the wavelet transform, variations in period and energy can be observed. In the SW band, two peak periods were identified (6 s and 12 s). The latter is the most powerful in low-tide situations. During high tide, this trend was reversed. In the IG and FIG bands, the period decreases at high tide and increases at low tide. As regards the IG band, WTA shows that the 90 s peak is more powerful in the first low tide and 45 s in high tide because the change in the water body, periods, and magnitude differ (Fig. 5). In the FFT, 6, 12, 45, 90, and 260 s peaks can be confirmed, and the last three are also confirmed in the MSP results.

For the surge analysis, Fig. 10 is presented. Color limits of wavelet transform differ from waves to make graphics legible. It is worth noting

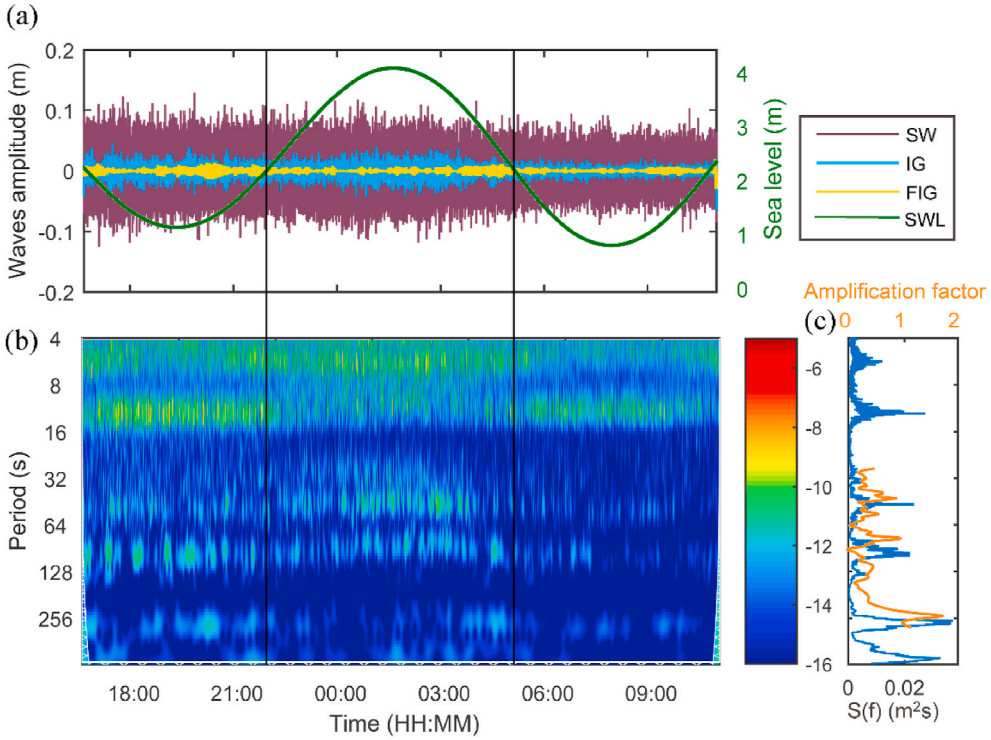

Fig. 9. (a) Time series and sea level, (b) Wavelet power spectrum, and (c) FFT of Miros radar during Scali del Teatro (ST_B) operation, on 03/18/2019 and 03/19/2019 at jetty 1.

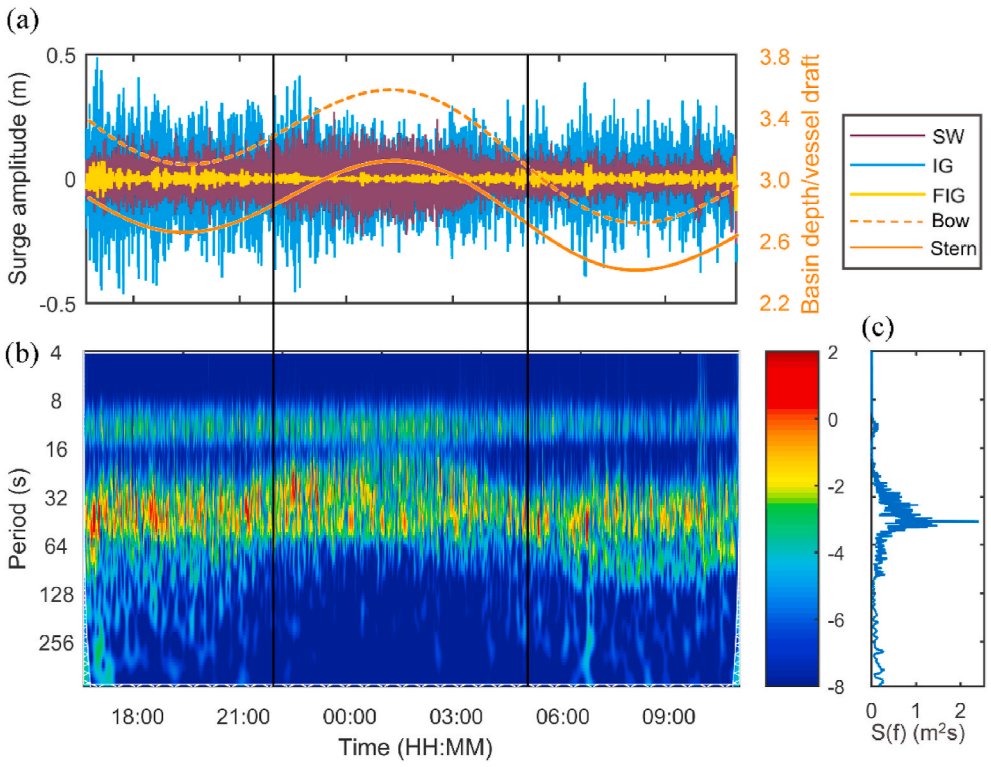

Fig. 10. (a) Time series and relation basin depth and vessel draft, (b) Wavelet power spectrum, and (c) FFT of surge motion of Scali del Teatro (ST_B) on 03/18/2019 and 03/19/2019 at jetty 1.

that during high tide, the IG waves reach the SW band. Consequently, the amplitudes could not be verified in the window filter records. This is attributed to the window filter process because the limit was set at 25 s (see Section 3).

The wavelet transform and FFT indicate peaks at two surge periods. The first in the SW band (12 s) remained during the monitoring period, in contrast to waves, which changed their peak period at high tide (6 s). However, the overall energy of this band is proportional (see Fig. 9). The second peak is the main peak of the surge motion (45 s).

As regards the IG band, the natural period of surge reaches higher values than the ones calculated, as the sea level is not considered in the formula. In the first low tide, it was close to 45 s, decreased at high tide

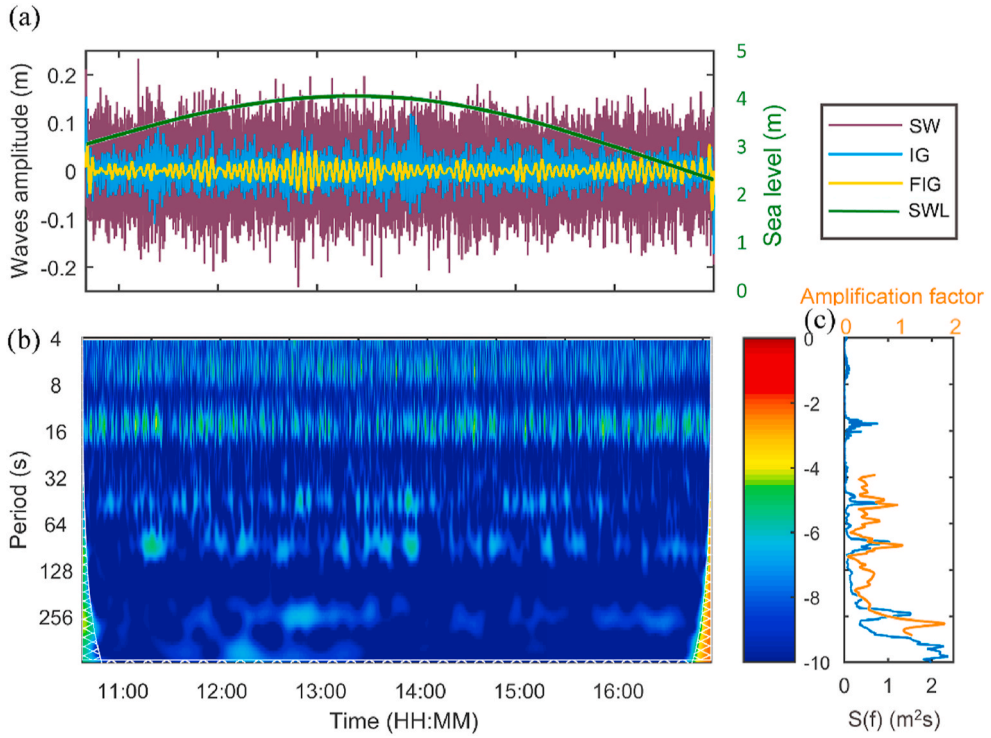

Fig. 11. (a) Time series (b) Wavelet power spectrum, and (c) FFT of Miros radar during SSL operation on 12/20/2018 at jetty 2.

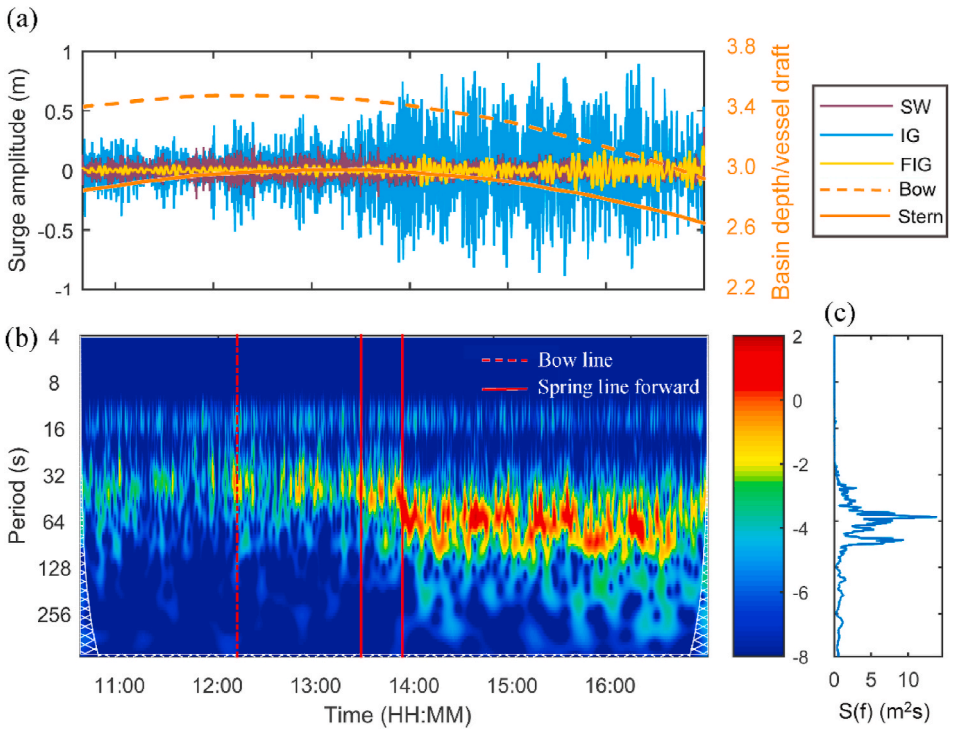

Fig. 12. (a) Time series (b) Wavelet power spectrum, and (c) FFT of surge motion of SSL on 12/20/2018 at jetty 2.

under 25 s, and increased in the second low tide above 60 s (the period increased with respect to the first low tide, as the vessel had more cargo inside). However, the energy packages of 45 s remained at all monitoring times. In FFT, this is the main peak, and dispersion is observed owing to the variability. As regards motion amplitudes, they are the highest in the first low tide because periods of the antinode next to this jetty (45 s) and surge match, causing resonance. The subsequent variation of the δ factor modifies the vessel period (but remains close); thus, the amplification is lower. Therefore, energy decreases during high tide and in the second low tide.

That is, the natural frequency of the surge motion is proportional to the δ factor. Furthermore, when the oscillation period of the vessel approaches the natural period of the basin, the ship motions become more energetic because they are excited by resonance. It was suggested by many authors, such as van der Molen and Ligteringen (2004) and Uzaki et al. (2010), and verified through WTA. Moreover, this phenomenon was observed in all the vessels and motions analyzed. This is especially relevant in the surge motion because its natural frequency of oscillation for this type of vessel is in the IG band.

To study not only resonance in the other location but also mooring influence, Figs. 11 and 12 show the waves and surge motion of the vessel SSL, respectively. The 6.5, 15, 45, 90, and 260 s peak periods are identified. Records maintained the same amplitudes, highlighting some energy packages. The same behavior is expected for horizontal motions. Nonetheless, surge motion behavior varies with time, and the spectrum is considered an exception compared with other vessels in Section 4.2, as shown in Fig. 7e. The reason for this can be seen in the wavelet transform of surge (Fig. 12), as shown below. Note that the SW and FIG bands did not show any representative peak period.

This vessel suffered three line breaks, as shown in Fig. 12b with vertical lines. They are attributed to the infragravity surge powerful packages. The first and second mooring breaks match with 1 m of motion amplitude and the third with 1.5 m, in any case doubling the average at that moment. However, this is not conclusive because other similar motion packages are recognized with no line break cases.

For better understanding, the figures were divided into three parts using line breaks: the first part before the bowline break, the second between the previous and the last line break, and the third after that. In the first part, the IG band shows the 45 s peak period and the lowest amplitudes. This period decreases in the second part to 30 s, owing to the highest tide, and the amplitudes increase. In the third part, the response changes drastically, as the period rises suddenly to 65 s, and the amplitude is more than double. Because the broken lines were replaced quickly, a plausible explanation is a change in the mooring pretension. Consequently, the basin mode and surge periods match, which leads to the resonant response of the vessel.

4.4. *Basin-vessel resonance and proposed operational thresholds*

The basin-vessel resonant response was observed in all analyzed vessels. This phenomenon can cause downtimes and even a lack of safety to stay at the berth. As exposed, ship motions are amplified when the basin and motion periods match. In this section, the influence of the

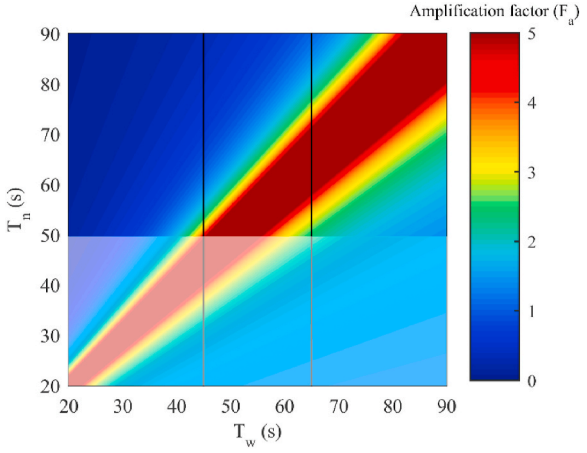

Fig. 13. Amplification factor in basin-vessel resonance. Vertical lines: main resonant modes in the inner jetty (45 s) and outer jetty (65 s). Dashed zone: range of surge natural periods of studied LGPs.

Table 5
Downtimes identified and significant wave height at Miros radar in the different frequency bands of respective sea states (1 h). H_s 45 corresponds to H_s of the 30–65 s band and H_s 90 corresponds to H_s of the 65–150 s band.

Jetty	Tanker	Vessel name	Length [m]	Date	H_s SW [m]	H_s IG + FIG [m]	H_s 45 [m]	H_s 90 [m]
1	LPG	B Gas Margrethe	100	12/20/2016 5:05	0.348	0.232	0.080	0.090
1	LPG	Scali Sanlorenzo	88	02/12/2018 2:42	0.199	0.153	0.077	0.078
2	LPG	Epic ST. Croix	100	03/04/2016 18:00	0.199	0.147	0.076	0.061
3	Crude Oil	Astra	272	02/06/2019 16:54	0.462	0.208	0.114	0.096
3	Crude Oil	Eagle Turin	247	11/08/2017 6:30	0.397	0.187	0.107	0.086
3	Crude Oil	Almi Navigator	274	02/09/2020 13:24	0.345	0.321	0.101	0.116
4	Oil	Iris Victoria	228	02/06/2019 16:24	0.462	0.208	0.114	0.096
4	Oil/Chemical	Aiolos	184	12/14/2020 1:00	0.247	0.188	0.099	0.068

relationship between both periods (basin-motion) was studied, and operational thresholds were proposed.

The 65 s is the main peak at the outer pressure gauge (next to jetty 2), instead of 45 s, which is the main peak at the intermediate gauge location (next to jetty 1), as shown in Fig. 3a. Consequently, vessels studied by wavelet transform resonate at different frequencies. The ST_B (jetty 1) resonates when its period matches 45 s and the SSL (jetty 2) when it matches 65 s.

The amplification factor of the ship motions, subject to a wave oscillation, $F_a = \frac{1}{\left|1-\left(\frac{T_n}{T_w}\right)^2\right|}$ is shown in Fig. 13, where T_n is the natural period of the motion and T_w is the basin period. The vertical lines are the resonant frequencies of the studied jetties, and the dashed zone shows the range of surge periods of this type of ship (16 s–48 s (section 4.1)). When the latter is considered, basin-vessel resonance in the inner jetty is more frequent because its frequency is in the range of this motion. However, vessels at the other jetty can reach the resonant period when spring tides occur, loaded, and/or low mooring pretension.

In resonance, the motions are higher when the energy of the wave spectrum in the frequency band of the motion increases. Therefore, the wave energy of the downtimes is analyzed.

Date and time information of downtimes at different berths of the oil terminal is available. Although vessel motions were unknown, it was possible to analyze the Miros radar records. Consequently, the record of the sea state (1 h) of each event was used to generate the spectrum. Subsequently, significant wave heights were obtained for different frequency bands: short-wave (SW), long-wave (IG + FIG), and those associated with the 45 s (range 30–65 s) and 90 s (range 65–150 s) peaks (Table 5).

Jetties 1 and 2 are adjacent to each other and berth similar vessels. Jetties 3 and 4 are located in a deeper area in parallel (Fig. 1d), docking other larger ships. Consequently, the downtimes of the vessels berthed in the first two jetties were analyzed separately from the vessels berthed at the others.

As regards the first ones, the B Gas Margrethe, Scali Sanlorenzo and Epic St. Croix vessels worked several hours prior to the interruption of the operation. In addition, it was observed that the forcers maintained their intensities. Moreover, the SW values varied for each case, whereas the wave height associated with the 45 s period was similar. Therefore, this indicates that downtimes occurred owing to a basin-vessel resonant problem.

Additionally, the SSL vessel (jetty 2), analyzed in Section 4.3, is studied here. In the monitoring process, H_s associated with the 45 s period (30–65 s band) were recorded from 0.071 m to 0.098 m, both before and during the resonance event. Despite the relevant amplification of the surge motion (Fig. 12), it can be assumed that this vessel did not interrupt its operation. Therefore, it should be noted that the decision for downtime is subjective. Notwithstanding, the analysis of the waves and the motions of this vessel allowed us to determine the situation generated by wave heights of the 30–65 s band higher than 0.071 m.

As regards jetties 3 and 4, the downtimes occurred again with different short-wave and long-wave heights (SW and IG + FIG). However, the wave height of the 30–65 s band (45 s peak) was approximately 0.1 m in the five cases. It should be noted that the swell increased slightly in both SW and long-wave magnitudes in the Astra and Iris Victoria cases. However, a stop was recorded when this limit was reached.

As expected, the higher the energy at frequencies close to the period of the vessel motion, the greater the motions generated in the resonance situation. As discussed, despite the variation in short and long waves between the different cases, the energy of the 30–65 s band is similar. This highlights the need and possibility of setting up a basin-vessel resonance threshold.

Based on the results obtained, an operational threshold of 0.076 m of 30–65 s H at the Miros radar is proposed for LPG vessels between 88 and 100 m in length. Additionally, the operational threshold of 0.1 m of 30–65 s wave height is accepted for jetties 3 and 4. It should be noted that these values are limited when the periods of motion of the ship are similar to some of the basin resonant modes. From these results, more research is needed to verify its application in other ports and set these thresholds for other types of vessels.

5. Conclusions

This work presents an integrated approach to assess basin-vessel resonance by combining real full-scale data in a synergetic manner ((Miros radar), pressure gauges, and ship motions), numerical modeling, and two post-processing methodologies: FFT and WTA. The measured vessel motions at two close berths in the oil terminal of the inner port of A Coruña (Spain) were studied along with wave analysis in a broad interval of frequencies, tide levels, and cargo loading conditions.

The results of the numerical model show that, due to the position of the nodes and antinodes, the resonant modes corresponding to the periods of 45 and 65 s are the most problematic for berths 1 and 2, respectively. The tide gauge records confirmed the harbor basin resonant frequencies are excited when sufficient wave energy is available. The resonance phenomenon was clearly observed for a significant height of the SW component above 0.12 m.

The natural surge period for LPG vessels was found to be in the interval of 16–48 s, depending on the characteristics of the mooring system (tension, life cycle, and material) and vessel displacements (loading condition). The higher periods of surge motion found at the outer jetty were explained by the use of newer and longer mooring lines at that berth, owing to the bollards position.

As regards vessel motions, spectral analysis shows that vessels with similar patterns in the SW range present more heave spectral density at the outer jetty, as they are more exposed. However, a surge is the main motion in the gravity and infragravity bands for ships berthed at the innermost jetty, which is considered the most critical motion by port operators.

The influence of the tide cycle was studied using information from the Miros radar through wavelet transform. The results show higher amplitudes of infragravity waves in high tides for 45 s waves, lower amplitudes for 90 s, and the opposite at low tides. As regards surge, it

was concluded that the oscillation period depends on the δ factor (δ = *water depth/vessel draft*), which involves tide level and loading conditions (lower tide levels and higher loads increase the surge period), and on the mooring system (configuration and pretension).

In addition, when the vessel motion frequency matches the energetic basin resonant mode at the berth, the amplitudes of the infragravity motions are amplified (resonance occurs). The three identified mooring breaks match, in time, with large infragravity surge motions (first and second with 1 m, and third with 1.5 m), which is doubled the average amplitude at those instants, whereas waves were kept constant.

The amplification factor of the resonance between the basin and the surge motions was analyzed. It was concluded that vessels at the inner jetty have more frequent resonant motions owing to their resonant mode at 45 s. This mode is in the surge resonant range for LPG vessels (19–45 s), in contrast to the other jetty (resonant mode at 65 s).

During resonance, when the wave energy in the frequency band of the motion period is higher, the amplifications are larger. Downtimes of eight vessels allowed the setting of long-wave operational thresholds for basin-vessel resonance. The wave height of the 30–65 s band, at Miros radar, is the limiting factor: 0.076 m for LPGs berthed at jetties 1 and 2 and 0.1 m for tankers docked at jetties 3 and 4.

CRediT authorship contribution statement

Raquel Costas: Conceptualization, Methodology, Validation, Formal analysis, Investigation, Data curation, Writing – original draft, Visualization. **Andrés Figuero:** Conceptualization, Investigation, Resources, Writing – review & editing, Supervision, Project administration, Funding acquisition. **Enrique Peña:** Conceptualization, Resources, Writing – review & editing, Supervision, Project administration, Funding acquisition. **José Sande:** Conceptualization, Resources, Writing – review & editing, Project administration, Funding acquisition. **Paulo Rosa-Santos:** Conceptualization, Writing – review & editing, Supervision.

Declaration of competing interest

The authors declare that they have no known competing financial interests or personal relationships that could have appeared to influence the work reported in this paper.

Acknowledgments

This research was funded by the Spanish Ministry of Economy, Industry, and Competitiveness, R&D National Plan (BIA2017-86738-R), Spanish Ministry of Science and Innovation, Retos Call, (PID2020-112794RB-I00 / AEI / 10.13039/501100011033), and the FPI predoctoral grant from the Spanish Ministry of Science, Innovation, and Universities (PRE2018-083777). Moreover, the principal author research stay with Professor Paulo Rosa-Santos was funded by AECT Galicia-North of Portugal with the IACOBUS Program–Research Stays, 6° Edition. Open access was funded by Universidade da Coruña/CISUG.

The authors are grateful to the Port Authority of A Coruña (Spain), REPSOL, the crew of reference vessels for their kind collaboration, Aquática for providing the pressure gauge data, and IHCantabria for the MSP model.

References

Bhautoo, P.S., 2017. Dynamic mooring analysis to investigate long period wave-induced vessel motions at Esperance Port. In: Australasian Coasts and Ports 2017 Conference, pp. 109–115.

Puertos del Estado. Spanish National Port Autority [WWW Document]. URL. http://www.puertos.es/es-es/oceanografia/Paginas/portus.aspx, 10.23.20.

Díaz-Hernández, G., 2006. Análisis de resonancia portuaria: generación, transitoriedad, no linealidad y acoplamiento geométrico. (Port resonance analysis: generation, transient, non-linearity and geometric coupling. Universidad de Cantabria.

EMODnet [WWW Document]. URL. https://www.emodnet-bathymetry.eu/, 5.10.21.

Figuero, Andrés, Rodriguez, A., Sande, J., Peña, E., Rabuñal, J.R., 2018a. Field measurements of angular motions of a vessel at berth: inertial device application. Control Eng. Appl. Informatics 20, 79–88.

Figuero, Andres, Rodriguez, A., Sande, J., Peña, E., Rabuñal, J.R., 2018b. Dynamical study of a moored vessel using computer vision. J. Mar. Sci. Technol. 26, 240–250. https://doi.org/10.6119/JMST.2018.04_(2).0011.

Figuero, A., Sande, J., Peña, E., Alvarellos, A., Rabuñal, J.R., Maciñeira, E., 2019. Operational thresholds of moored ships at the oil terminal of inner port of A Coruña (Spain). Ocean Eng. 172, 599–613. https://doi.org/10.1016/j.oceaneng.2018.12.031.

Gao, J., Ma, Xiaozhou, Zang, J., Dong, G., Ma, Xiaojian, Zhu, Y., Zhou, L., 2020. Numerical investigation of harbor oscillations induced by focused transient wave groups. Coast. Eng. 158 https://doi.org/10.1016/j.coastaleng.2020.103670.

García-Valdecasas, J., Pérez Gómez, B., Molina, R., Rodríguez, A., Rodríguez, D., Pérez, S., Campos, Á., Rodríguez Rubio, P., Gracia, S., Ripollés, L., Terrés Nicoli, J. M., de los Santos, F.J., Álvarez Fanjul, E., 2021. Operational tool for characterizing high-frequency sea level oscillations. Nat. Hazards 106, 1149–1167. https://doi.org/10.1007/s11069-020-04316-x.

González-Marco, D., Sierra, J.P., Fernández de Ybarra, O., Sánchez-Arcilla, A., 2008. Implications of long waves in harbor management: the Gijón port case study. Ocean Coast Manag. 51, 180–201. https://doi.org/10.1016/j.ocecoaman.2007.04.001.

Gourlay, T.P., 2019. A coupled ship and harbour model for dynamic mooring analysis in Geraldton harbour. In: Australasian Coasts and Ports 2019 Conference. Hobart, pp. 471–477.

Gulshan, Kumar, P., Rajni, 2020. Moored ship motion analysis in Paradip port under the resonance conditions using 3-D boundary element method. J. Mar. Sci. Technol. M. https://doi.org/10.1007/s00773-020-00701-0.

Hiraishi, T., 1997. Observation of Long Period Wave and Ship Motion in Tomalomai-Port.

Huang, M.C., 2004. Wave parameters and functions in wavelet analysis with filtering. Ocean Eng. 31, 813–831. https://doi.org/10.1016/j.oceaneng.2003.10.004.

Kumar, P., Gulshan, 2018. Theoretical analysis of extreme wave oscillation in Paradip Port using a 3-D boundary element method. Ocean Eng. 164, 13–22. https://doi.org/10.1016/j.oceaneng.2018.06.029.

Kumar, P., Zhang, H., Ik Kim, K., Yuen, D.A., 2016. Modeling wave and spectral characteristics of moored ship motion in Pohang New Harbor under the resonance conditions. Ocean Eng. 119, 101–113. https://doi.org/10.1016/j.oceaneng.2016.04.027.

Kwak, M., Pyun, C., 2013. Computer simulation of moored ship motion considering harbor resonance in Pohang new harbor. https://doi.org/10.1061/9780784413067.145, 1415-1424.

Leys, V., Fernandez, V., Kolijn, D., 2018. Resonant oscillations in small craft harbours: observations and mitigation modeling examples from Atlantic Canada. Proc. Coast. Eng. Conf. 36, 1–7.

Liu, Y., Liang, Y., Weisberg, R.H., 2007. Rectification of the bias in the wavelet power spectrum. https://doi.org/10.1175/2007JTECHO511.1.

Liu, X., Liu, H., Guo, Q., Zhang, C., 2020. Adaptive wavelet transform model for time series data prediction. Soft Comput. 24, 5877–5884. https://doi.org/10.1007/s00500-019-04400-w.

López, M., Iglesias, G., 2014. Long wave effects on a vessel at berth. Appl. Ocean Res. 47, 63–72. https://doi.org/10.1016/j.apor.2014.03.008.

López, M., Iglesias, G., Kobayashi, N., 2012. Long period oscillations and tidal level in the Port of Ferrol. Appl. Ocean Res. 38, 126–134. https://doi.org/10.1016/j.apor.2012.07.006.

Lorente, P., Sotillo, M.G., Aouf, L., Amo-Baladrón, A., Barrera, E., Dalphinet, A., Toledano, C., Rainaud, R., De Alfonso, M., Piedracoba, S., Basañez, A., García-Valdecasas, J.M., Pérez-Muñuzuri, V., álvarez-Fanjul, E., 2018. ExtremeWave height events in NW Spain: a combined multi-sensor and model approach. Rem. Sens. 10, 1–12. https://doi.org/10.3390/rs10010001.

Loughlin, P., Cohen, L., 2010. Wavelets: a comparison with the spectrogram and other methods for time-frequency analysis. J. Acoust. Soc. Am. 127, 1936. https://doi.org/10.1121/1.3384871.

Massel, S.R., 2001. Wavelet analysis for processing of ocean surface wave records. Ocean Eng. 28, 957–987. https://doi.org/10.1016/S0029-8018(00)00044-5.

Miros radar [WWW Document]. URL. https://www.miros-group.com/products/, 5.31.21.

Molavi, A., Lim, G.J., Race, B., 2019. A framework for building a smart port and smart port index. Int. J. Sustain. Transp. 14, 686–700. https://doi.org/10.1080/15568318.2019.1610919.

MSP [WWW Document]. URL. http://archivo.ihcantabria.com/index.php/item/680-msp, 9.25.20.

PIANC, 1995. Criteria for Movements of Moored Ships in Harbours - A Practical Guide.

Puertos del Estado, 2011. ROM 2.0-11. Recomendaciones para el proyecto y ejecución en Obras de Atraque y Amarre. Puertos del Estado.

Puertos del Estado, 2021. Autoridad Portuaria de A Coruña. Puertos del Estado [WWW Document]. A Coruña Port Auth. URL. http://cma.puertocoruna.com/, 10.23.20.

Reniers, A.J.H.M., Naporowski, R., Tissier, M.F.S., de Schipper, M.A., Akrish, G., Rijnsdorp, D.P., 2021. North sea infragravity wave observations. J. Mar. Sci. Eng. 9, 1–19. https://doi.org/10.3390/jmse9020141.

Rhif, M., Abbes, A. Ben, Farah, I.R., Martínez, B., Sang, Y., 2019. Wavelet transform application for/in non-stationary time-series analysis: a review. Appl. Sci. 9, 1–22. https://doi.org/10.3390/app9071345.

Rosa-Santos, P., Taveira-Pinto, F., Veloso-Gomes, F., 2014. Experimental evaluation of the tension mooring effect on the response of moored ships. Coast. Eng. 85, 60–71. https://doi.org/10.1016/j.coastaleng.2013.11.012.

Sakakibara, S., Kubo, M., 2008. Effect of mooring system on moored ship motions and harbour tranquillity. Int. J. Ocean Syst. Manag. 1, 84–99.
Santos, J.A., Pinheiro, L.V., Abdelwahab, H.S., Fortes, C.J.E.M., Pedro, F.G.L., Capitão, R. P., Hinostroza, M.A., Soares, C.G., 2019. Physical modelling of motions and forces on a moored ship at the leixões port. Defect diffus. Forum 396, 60–69. https://doi.org/10.4028/www.scientific.net/DDF.396.60.
Sasa, K., Mitsui, M., Tamura, M., 2018. Survey and analysis on safety of ship mooring operations on Japanese ports facing open seas. In: 37th International Conference on Ocean. Offshore and Arctic Engineering, Madrid, pp. 1–9.
Shi, X.Y., Zhang, N.C., Chen, C.P., Jiang, H.Z., Cui, L., 2014. Experimental study of characteristics of motions of a large mooring ship in long-period waves. J. Mar. Sci. Technol. 22, 240–246. https://doi.org/10.6119/JMST-013-0606-2.
Sorensen, R., Thompson, E.F., 2008. Harbor hydrodynamics. In: Coastal Engineering Manual, pp. 34–37. https://doi.org/10.20622/jltaj.11.0_toc1.
Tharanga, D., 2014. Harbour Oscillations: Generation and Minimisation of Their Impacts.
Thotagamuwage, D.T., Pattiaratchi, C.B., 2014. Observations of infragravity period oscillations in a small marina. Ocean Eng. 88, 435–445. https://doi.org/10.1016/j.oceaneng.2014.07.003.
Torrence, C., Compo, G.P., 1998. A partical guide to wavelet analysis. Bull. Amreican Meteorol. Soc. 79, 61–78. https://doi.org/10.1175/1520-0477(1998)079<0061:Apgtwa>2.0.Co;2.
Troch, C., Terblanche, L., Henning, H., 2020. Modelling and measurement of low-frequency surge motion associated with extreme storm conditions in the Port of Cape Town. Appl. Ocean Res. 102452. https://doi.org/10.1016/j.apor.2020.102452.
UNCTAD, 2020. Review of Maritime Transport 2020.
Uzaki, K. ichi, Matsunaga, N., Nishii, Y., Ikehata, Y., 2010. Cause and countermeasure of long-period oscillations of moored ships and the quantification of surge and heave amplitudes. Ocean Eng. 37, 155–163. https://doi.org/10.1016/j.oceaneng.2009.12.004.
van der Molen, W., Ligteringen, H., 2004. Influence of loading condition on the behavior of a moored liquefied natural gas ship. J. Waterw. Port, Coast. Ocean Eng. 131, 33–36. https://doi.org/10.1061/(asce)0733-950x(2005)131:1(33).
van der Molen, W., Monárdez, P., van Dongeren, A., 2006. Numerical simulation of long-period waves and ship motions in tomakomai port, Japan. Coast Eng. J. 48, 59–79. https://doi.org/10.1142/s0578563406001301.
van Deyzen, A.F.J., Beimers, P.B., van Der Lem, J.C., Messiter, D., De Bont, J.A.M., 2015. To improve the efficiency of ports exposed to swell. In: Aust. Coasts Ports 2015 Conf, pp. 919–926.
van Dongeren, A., de Jong, M., van der Lem, C., van Deyzen, A., den Bieman, J., 2016. Review of long wave dynamics over reefs and into ports with implication for port operations. J. Mar. Sci. Eng. 4 https://doi.org/10.3390/jmse4010012.
Wang, H., Wolgamot, H.A., Draper, S., Zhao, W., Taylor, P.H., Cheng, L., 2019. Resolving wave and laminar boundary layer scales for gap resonance problems. J. Fluid Mech. 866, 759–775. https://doi.org/10.1017/jfm.2019.115.
Yoneyama, H., Shiraishi, S., Satoh, H., 2004. Experimental verification of a reduction system for low-frequency ship motions and examination for its practical use. In: Oceans '04 MTS/IEEE Techno-Ocean '04. IEEE Cat. No.04CH37600), Kobe, pp. 1121–1128. https://doi.org/10.1109/oceans.2004.1405667.
Yu, Y., Shenoi, R.A., Zhu, H., Xia, L., 2006. Using wavelet transforms to analyze nonlinear ship rolling and heave-roll coupling. Ocean Eng. 33, 912–926. https://doi.org/10.1016/j.oceaneng.2005.05.014.
Zhang, T., Zheng, X., Liu, M., 2021. Multiscale attention-based LSTM for ship motion prediction. Ocean Eng. 230, 109066. https://doi.org/10.1016/j.oceaneng.2021.109066.
Zhao, W., Wolgamot, H.A., Taylor, P.H., Eatock Taylor, R., 2017. Gap resonance and higher harmonics driven by focused transient wave groups. J. Fluid Mech. 812, 905–939. https://doi.org/10.1017/jfm.2016.824.